

## Original Article

# Preparation of conducting polymer polyaniline/g-C<sub>3</sub>N<sub>4</sub> heterojunction for enhanced CO<sub>2</sub> photoreduction into fuel

Yujuan Liu, Suping Wang, Kejun Bi\*, Yapo Sun

Intelligent Construction School, Zhengzhou Business University, Zhengzhou, Henan, China

## ARTICLE INFO

### Keywords:

Graphite phase carbon nitride  
Photocatalytic reduction of CO<sub>2</sub>  
Polyaniline  
Z scheme heterojunction

## ABSTRACT

The g-C<sub>3</sub>N<sub>4</sub>/polymer polyaniline (g-C<sub>3</sub>N<sub>4</sub>/PANI) is synthesized using constructing heterojunction strategy for CH<sub>3</sub>OH production by CO<sub>2</sub> photoreduction. The CO<sub>2</sub> photoreduction performance for CH<sub>3</sub>OH production of g-C<sub>3</sub>N<sub>4</sub>/PANI was investigated by regulating PANI content. The construction of the heterojunction effectively promotes the separation of photogenerated carriers with a high charge transfer rate, contributing to CO<sub>2</sub> photoreduction. Besides, the incorporation of the PANI layer enhances electron transfer efficiency and improves CO<sub>2</sub> adsorption capacity. The g-C<sub>3</sub>N<sub>4</sub>/PANI also exhibits good selectivity for CH<sub>3</sub>OH production, with a selectivity of 95.26%. The g-C<sub>3</sub>N<sub>4</sub>/PANI still maintains excellent CO<sub>2</sub> photoreduction activity after cycles. The mechanism of the CH<sub>3</sub>OH production from CO<sub>2</sub> photoreduction is analyzed through the energy band structure.

## 1. Introduction

With the advancement of industrialization and the growth of population, the demand for energy continues to grow, and fossil fuels such as coal, oil, and natural gas are consumed in large quantities [1]. The burning of fossil fuels will emit large amounts of CO<sub>2</sub>, triggering environmental problems such as global warming, leading to rising sea levels and melting of polar ice and snow, which has had a serious impact on the ecological environment and human production and living order [1]. Besides, the intensification of extreme weather events has become increasingly evident across the globe, with rising frequencies and severities of droughts and heavy precipitation episodes. Therefore, how to achieve efficient utilization of the greenhouse gas CO<sub>2</sub> has become very important. Currently, CO<sub>2</sub> is mainly utilized through mineralization storage, biological transformation, chemical adsorption, and catalytic reduction [2]. Through catalytic reduction, CO<sub>2</sub> is reduced to products such as methane, formic acid, and methanol. These products can be directly used as fuel for fuel cells, realizing the conversion of chemical energy into electrical energy, which can not only effectively alleviate the energy crisis but also reduce environmental pollution [3]. The reduction of CO<sub>2</sub> can be driven by light energy, electrical energy, and thermal energy. Photocatalysis has the characteristics of high efficiency and greenness and has good potential applications in the field of CO<sub>2</sub> reduction. However, the bond energy of the C-O bond of CO<sub>2</sub> reaches as high as 750 kJ·mol<sup>-1</sup>, which makes CO<sub>2</sub> reduction still a certain challenge [4]. Consequently, preparing efficient and stable materials for photocatalytic CO<sub>2</sub> reduction is of critical importance.

The g-C<sub>3</sub>N<sub>4</sub>, as an excellent semiconductor photocatalytic material, has good chemical stability, simple preparation, and good visible optical response capabilities [5,6]. The g-C<sub>3</sub>N<sub>4</sub> has found extensive application

in environmental remediation for the degradation of organic pollutants, nitrogen oxides, and formaldehyde. Besides, it is also used in the field of new energy for photodegradation of water to produce H<sub>2</sub> or photocatalytic reduction of CO<sub>2</sub> to generate methanol [7,8]. However, the photogenerated carriers of the g-C<sub>3</sub>N<sub>4</sub> are seriously recombined, which greatly limits the CO<sub>2</sub> photoreduction for the production of methanol [9]. Therefore, the g-C<sub>3</sub>N<sub>4</sub> should be modified to restrain the recombination of photogenerated carriers to realize the efficient CO<sub>2</sub> photoreduction.

Currently, common modification strategies include co-catalysts [10], morphology modulation [11], elemental doping [12], and construction of heterojunctions [13] for improving the CO<sub>2</sub> photoreduction performance of the g-C<sub>3</sub>N<sub>4</sub> for methanol production. Among these modification methods, the construction of heterojunctions, including g-C<sub>3</sub>N<sub>4</sub>/TiO<sub>2</sub> [14], ZnO/g-C<sub>3</sub>N<sub>4</sub> [15], and MoS<sub>2</sub>/g-C<sub>3</sub>N<sub>4</sub> [16], is regarded as an efficient strategy for solving the photogenerated carrier recombination of the g-C<sub>3</sub>N<sub>4</sub>. Song *et al.* prepared a multifunctional g-C<sub>3</sub>N<sub>4</sub>-PDI heterojunction for enhanced CO<sub>2</sub> reduction with excellent photocatalytic performance [17]. The formation of a heterojunction not only improves CO<sub>2</sub> adsorption but also accelerates the migration of photogenerated electrons, playing a crucial role in CO<sub>2</sub> photoreduction. Ma *et al.* synthesized Au/g-C<sub>3</sub>N<sub>4</sub>/CdS heterojunction for CO<sub>2</sub> photoreduction, indicating that the formed heterojunction speeds up the carriers' separation efficiency [18]. Therefore, the construction of a heterojunction can improve the CO<sub>2</sub> photoreduction performance of the g-C<sub>3</sub>N<sub>4</sub>.

Organic semiconductors, as a class of conductive polymers, exhibit several distinctive properties, including being metal-free, possessing high stability, electrical conductivity, biocompatibility, and environmental friendliness [19-20]. Common organic semiconductors encompass a

### \*Corresponding author:

E-mail address: [xauat2025@163.com](mailto:xauat2025@163.com) (K. Bi)

Received: 02 March, 2025 Accepted: 28 October, 2025 Epub Ahead of Print: 10 February, 2026 Published: 02 March, 2026

DOI: 10.25259/AJC\_217\_2025

This is an open-access article distributed under the terms of the Creative Commons Attribution-Non Commercial-Share Alike 4.0 License, which allows others to remix, transform, and build upon the work non-commercially, as long as the author is credited and the new creations are licensed under the identical terms.

range of conductive polymers, including polyaniline, polydopamine, polypyrrole, and polyacrylonitrile [21]. Among these organic semiconductors, the polyaniline (PANI) exhibits excellent electrical conductivity and photothermal conversion properties, facilitating free electron migration due to its extensive internal  $\pi$ - $\pi$  conjugation system [22-23]. Miao *et al.* (2023) prepared the AuCu/PANI/g-C<sub>3</sub>N<sub>4</sub> heterostructure for enhanced CO<sub>2</sub> photoreduction, indicating that the PANI layer enhances CO<sub>2</sub> adsorption and accelerates charge transfer with excellent photocatalytic reduction performance of CO<sub>2</sub> [24]. However, the preparation process of AuCu/PANI/g-C<sub>3</sub>N<sub>4</sub> heterostructure is complex and expensive, which limits large-scale preparation and application. Therefore, it is of great significance to develop low-cost and easy-to-prepare photocatalysts that reduce CO<sub>2</sub> to methanol [25]. Relevant studies have demonstrated that PANI can improve the separation of photogenerated carriers and function as efficient energy band modulators [25]. Besides, PANI exhibits excellent photostability and thermal stability, ensuring the recyclability of photocatalysts [26]. Therefore, preparing the PANI/g-C<sub>3</sub>N<sub>4</sub> heterostructure can improve its capacity for enhanced CO<sub>2</sub> photoreduction by improving light utilization and CO<sub>2</sub> adsorption, and accelerating charge transfer.

The coupling of the g-C<sub>3</sub>N<sub>4</sub> with the conductive polymer PANI is achieved through the strategy of constructing a heterojunction with good selectivity for CH<sub>3</sub>OH production. The preparation process of the PANI/g-C<sub>3</sub>N<sub>4</sub> is simple, which is conducive to industrial utilization. Physicochemical properties of PANI/g-C<sub>3</sub>N<sub>4</sub> were analyzed. CO<sub>2</sub> photoreduction performance of PANI/g-C<sub>3</sub>N<sub>4</sub> was optimized by modulating PANI content under visible light irradiation. The formed heterojunction improves the light utilization and accelerates the charge separation. The PANI/g-C<sub>3</sub>N<sub>4</sub> exhibited excellent CO<sub>2</sub> photoreduction performance compared to g-C<sub>3</sub>N<sub>4</sub>. A possible mechanism was put forward to analyze the enhanced photocatalytic performance for CO<sub>2</sub> reduction. This research provides a new approach for designing photocatalysts aimed at CO<sub>2</sub> photoreduction.

## 2. Materials and Methods

### 2.1. Experimental material

Melamine (C<sub>3</sub>H<sub>6</sub>N<sub>6</sub>), potassium bromide (KBr), sodium sulphate (Na<sub>2</sub>SO<sub>4</sub>), barium sulphate (BaSO<sub>4</sub>), ammonium persulphate ((NH<sub>4</sub>)<sub>2</sub>S<sub>2</sub>O<sub>8</sub>), anhydrous ethanol (C<sub>2</sub>H<sub>5</sub>OH), aniline (C<sub>6</sub>H<sub>7</sub>N), sulphuric acid (H<sub>2</sub>SO<sub>4</sub>), are purchased from Aladdin Reagent Co. All the medicines are not further purified.

### 2.2. Preparation of PANI/g-C<sub>3</sub>N<sub>4</sub>

The g-C<sub>3</sub>N<sub>4</sub> was prepared by in situ thermal polymerization [27]. For this, 5 g of melamine were placed in a porcelain boat and subsequently transferred to the muffle furnace. The sample was heated under a nitrogen atmosphere at 15°C·min<sup>-1</sup> to 540°C for 3 h. Afterward, the residue in the muffle furnace was naturally cooled to room temperature; this residue was g-C<sub>3</sub>N<sub>4</sub>.

The g-C<sub>3</sub>N<sub>4</sub>/PANI (3%) heterostructure was prepared as follows. Firstly, 0.5 g g-C<sub>3</sub>N<sub>4</sub> was homogeneously added into 10 mL H<sub>2</sub>SO<sub>4</sub> (0.05 mol·L<sup>-1</sup>). Secondly, 0.015 g of aniline and 0.10 g of ammonium persulfate were added at a temperature of -5-0°C, which was stirred for 12 h and then filtered. Finally, the g-C<sub>3</sub>N<sub>4</sub>/PANI (3%) heterostructure was washed using deionized water and anhydrous ethanol, and then dried at 60°C for 24 h. According to the above-mentioned method, the g-C<sub>3</sub>N<sub>4</sub>/PANI (1% or 5%) heterostructure was prepared by adjusting the dosage of aniline, and PANI was prepared without adding g-C<sub>3</sub>N<sub>4</sub>.

### 2.3. Characterization

The physical phase and crystal of the sample were characterized by a Bruker D8 QUEST ECO X-ray diffraction (XRD) instrument (K $\alpha$  Cu target, tube voltage 40 kV, current 40 mA, 2 $\theta$  =10-40°). The composition and structure of the sample were characterized by a Thermo Nicolet I550 infrared spectrum using the KBr compression method. The morphology and elemental composition of the sample were analyzed using Zeiss GeminiSEM 460 scanning electron microscopy (SEM),

Hitachi HT-7700 transmission electron microscopy (TEM), and a high-angle ring hidden field projection electron microscope. The element composition of the sample was characterized using the Shimadzu Axis Nova X-ray optoelectronics spectrum (the K $\alpha$  Al source, the voltage of 5.0 kV, the power of 600 W). The spectrum response of the sample was characterized by the Agilent Cary 3500 UV visible reflectance spectrometer (BaSO<sub>4</sub> reference, the scanning range 220-800 nm). The photogenerated carrier recombination and lifetimes of the sample were characterized by a Thermo ARL 9900 photoluminescence spectrometer. The photocurrent intensity and AC impedance of the sample were determined by the Zahner Zennium pro electrochemical workstation. The test system was composed of a Pt electrode, an AgCl/Ag electrode, and an FTO electrode. The electrolyte was Na<sub>2</sub>SO<sub>4</sub> solution with 0.1 mol·L<sup>-1</sup>.

### 2.4. CO<sub>2</sub> photoreduction for production of CH<sub>3</sub>OH

The photocatalytic experimental device is the Zhongke Micro Energy CME-PC6 photochemical reactor. The light source is a 500 W Xe lamp ( $\lambda$ >420 nm) to simulate visible light. The light source is 20 cm away from the liquid surface, and the average illumination intensity of the liquid surface is 60 $\mu$ W·cm<sup>-2</sup>. The reaction temperature is 25°C, and the visible light photocatalytic reduction performance of CO<sub>2</sub> by the g-C<sub>3</sub>N<sub>4</sub>/PANI composite is evaluated. Firstly, 50 mg of the photocatalyst is evenly dispersed into a cylindrical stainless steel photocatalytic reactor containing 20 mL of deionized water, stirred magnetically, bubbled with high-purity CO<sub>2</sub> (99.999%) gas for 10 min to discharge the air, and the outlet valve is closed. Secondly, high-purity CO<sub>2</sub> is introduced and the flow rate is controlled at 50 mL·min<sup>-1</sup>. When the CO<sub>2</sub> pressure in the reactor reaches about 1.0 atm, CO<sub>2</sub> is stopped, the Xe lamp is turned on, and the reaction time is 4 h. Finally, the gas-liquid products are analyzed by an Agilent 7890B high-performance gas chromatograph equipped with an FID detector (Porapak Q column, TCD detector) to determine product composition and yield. The yield (product formation rate) is calculated according to Eq. (1).

$$R_{\text{Product}} = \frac{n_{\text{Product}}}{m \times t} \quad (1)$$

$R_{\text{Product}}$  : the product generation rate,  $\mu\text{mol} \cdot \text{g}^{-1} \cdot \text{h}^{-1}$ ;  
 $n_{\text{Product}}$  : the amount of product substance,  $\mu\text{mol}$ ;  
 $m$ : the amount of catalyst, g;  
 $t$ : the reaction time, h

## 3. Results and Discussion

### 3.1. X-ray diffraction and Fourier transform infrared analysis

The physical phase and crystal of PANI, g-C<sub>3</sub>N<sub>4</sub>, and g-C<sub>3</sub>N<sub>4</sub>/PANI are characterized (Figure 1a). As displayed in Figure 1(a), diffraction peaks at 12.9° and 27.6° correspond to the (100) and (002) crystal planes of g-C<sub>3</sub>N<sub>4</sub>, respectively [28]. The existence of the (100) plane is associated with the s-triazine ring. The (002) plane is attributed to the lamellar stacking of carbon-nitrogen aromatic heterocyclic rings [29]. The (011), (020), and (200) crystal surfaces of PANI appear at 2 $\theta$ =15.4°, 20.4°, and 24.9°[30]. The XRD pattern of g-C<sub>3</sub>N<sub>4</sub>/PANI exhibits near consistency with the g-C<sub>3</sub>N<sub>4</sub>, which is mainly due to the weak crystallinity and low content of PANI. Therefore, the incorporation of the PANI doesn't modify the crystalline structure of g-C<sub>3</sub>N<sub>4</sub>. With increasing in PANI content, the intensity of the diffraction peak at 2 $\theta$ =12.9° and 27.6° gradually weakens. This result indicates that the g-C<sub>3</sub>N<sub>4</sub> is wrapped by the conductive polymer PANI. The average grain sizes of g-C<sub>3</sub>N<sub>4</sub>, g-C<sub>3</sub>N<sub>4</sub>/PANI (1%), g-C<sub>3</sub>N<sub>4</sub>/PANI (3%), and g-C<sub>3</sub>N<sub>4</sub>/PANI (5%) composites are calculated by the Debye-Scherrer equation to be 8.92, 8.11, 7.97, and 7.89 nm, respectively. This result indicates that the grain size of g-C<sub>3</sub>N<sub>4</sub> is reduced after PANI wrapping. The reason for this result may be the formation of chemical bonding between the PANI and g-C<sub>3</sub>N<sub>4</sub> interface, thereby forming a heterojunction, resulting in lattice distortion and inhibiting the growth of grains [31].

The surface functional group of PANI, g-C<sub>3</sub>N<sub>4</sub>, and g-C<sub>3</sub>N<sub>4</sub>/PANI is characterized by Fourier transform infrared (FTIR) (Figure 1b). The absorption bands of g-C<sub>3</sub>N<sub>4</sub> at 3000-3500 cm<sup>-1</sup>, attributed to -NH<sub>2</sub> and

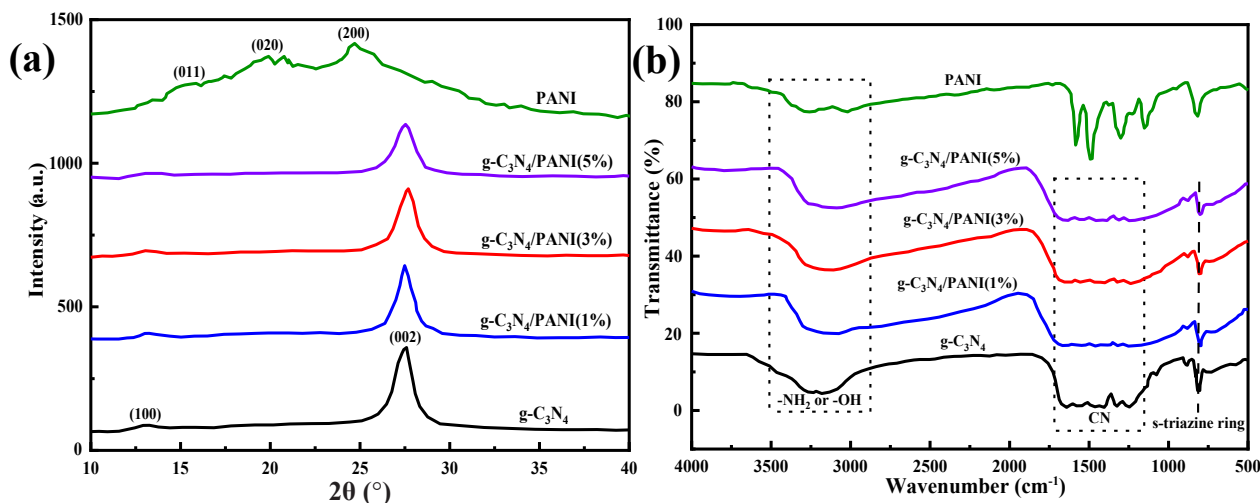


**Figure 1.** (a) XRD and (b) FTIR spectra of PANI,  $g\text{-C}_3\text{N}_4$ , and  $g\text{-C}_3\text{N}_4/\text{PANI}$ .

-OH groups, are associated with the incomplete polymerization of the melamine precursor and adsorbed  $\text{H}_2\text{O}$ . The absorption bands at  $1200\text{--}1650\text{ cm}^{-1}$  correspond to stretching vibrations of  $\text{C}=\text{N}$  and  $\text{C}-\text{N}$  bonds within the carbon-nitrogen rings. While the deformation vibration of the s-triazine ring appears at  $809\text{ cm}^{-1}$  [32]. The stretching vibrations of aromatic rings and benzene ring  $\text{C}=\text{C}$  of the PANI appear at  $1498$  and  $1582\text{ cm}^{-1}$ , respectively. The absorption band at  $1304\text{ cm}^{-1}$  is a  $\text{C}-\text{N}$  stretching vibration. The absorption bands at  $1156\text{ cm}^{-1}$  and  $827\text{ cm}^{-1}$  correspond to the  $=\text{NH}^+$  and the  $\text{C}-\text{H}$  stretching vibration outside the benzene ring face, respectively [33]. The  $g\text{-C}_3\text{N}_4/\text{PANI}$  exhibits an FTIR pattern nearly identical to the pristine  $g\text{-C}_3\text{N}_4$ . However, the absorption band intensity gradually weakens as PANI content increases due to the fact that  $g\text{-C}_3\text{N}_4$  is encapsulated by the PANI. This result is consistent with XRD analysis.

### 3.2. Micro-morphological analysis

As Figure 2(a) shows,  $g\text{-C}_3\text{N}_4$  has a typical layer-stacked 2D nanosheet structure with a relatively rough surface. PANI is polymerized in situ onto  $g\text{-C}_3\text{N}_4$  nanosheets, resulting in a smooth surface (Figure 2b). The white arrows of the Figure 2(b) denote the PAN and  $g\text{-C}_3\text{N}_4$ , respectively. Besides, the conductive polymer PANI uniformly covers the  $g\text{-C}_3\text{N}_4$  surface. Morphology of  $g\text{-C}_3\text{N}_4/\text{PANI}$  is further observed and analyzed

by TEM and HAADF-STEM (Figure 2c,d). As Figures 2(c,d) shown, the conductive polymer PANI also uniformly coats the  $g\text{-C}_3\text{N}_4$  surface. The “dark” part of the HAADF-STEM image is  $g\text{-C}_3\text{N}_4$ , and the “bright” part proves that  $g\text{-C}_3\text{N}_4$  is uniformly wrapped by the conductive polymer PANI (Figure 2d). Figures 2(e,f) show the EDS images of the  $g\text{-C}_3\text{N}_4/\text{PANI}$ . As Figure 2(e,f) shows, the C and N elements in  $g\text{-C}_3\text{N}_4/\text{PANI}$  exhibit a dense distribution.

### 3.3. XPS analysis

The elemental compositions of  $g\text{-C}_3\text{N}_4$  and  $g\text{-C}_3\text{N}_4/\text{PANI}(3\%)$  were characterized using XPS spectra. As Figure 3(a) shows, the binding energies at  $284.4$ ,  $287.1$ , and  $287.6$  correspond to the  $\text{C}-\text{C}$ ,  $\text{C}-\text{N}$ , and  $\text{N}=\text{C}-\text{N}$  groups, respectively. Additionally, the peak near  $292.9\text{ eV}$  corresponds to the characteristic peak of  $\pi\text{-}\pi^*$  conjugation [34]. The binding energy at  $283.9\text{ eV}$  corresponds to the characteristic peak of  $\text{sp}^3$ -hybridized heterocyclic carbon ( $\text{C}-\text{C}$  or  $\text{C}-\text{H}$ ) in the conductive polymer PANI. The binding energy at  $285.7\text{ eV}$  corresponds to the  $\text{sp}^3$ -hybridized heterocyclic carbon ( $\text{C}-\text{N}$ ) in the conductive polymer PANI [35]. The  $\text{C} 1\text{s}$  characteristic peak of  $g\text{-C}_3\text{N}_4/\text{PANI}$  exhibits a shift toward higher binding energy compared to pristine  $g\text{-C}_3\text{N}_4$ . This result indicates that it exists a strong interaction between PANI and  $g\text{-C}_3\text{N}_4$ . This interaction serves as the foundation for charge transfer.

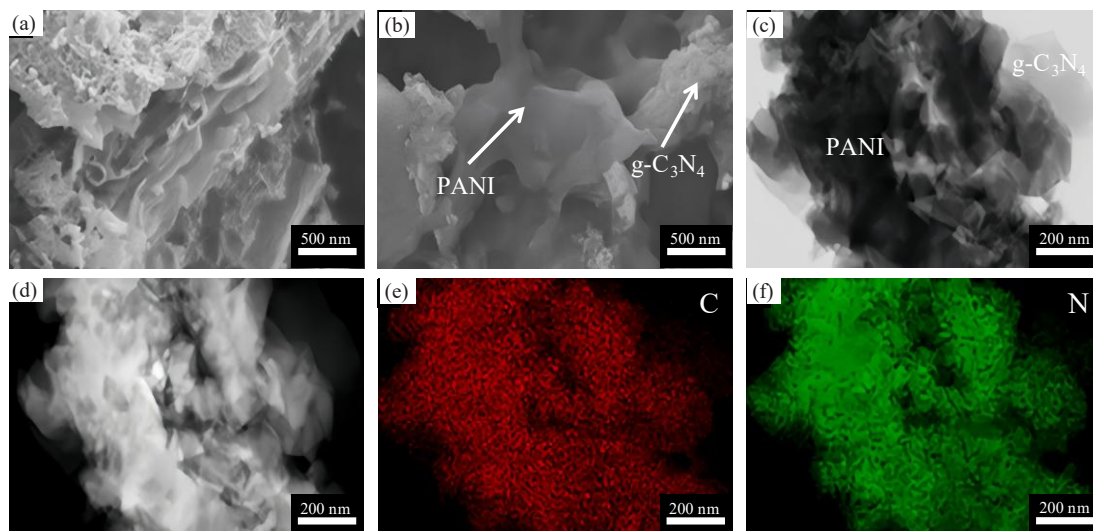


**Figure 2.** SEM (a) of  $g\text{-C}_3\text{N}_4$  and (b)  $g\text{-C}_3\text{N}_4/\text{PANI}(3\%)$ . The white arrows denote the PAN and  $g\text{-C}_3\text{N}_4$ , respectively. (c) TEM, (d) HAADF-STEM of  $g\text{-C}_3\text{N}_4/\text{PANI}(3\%)$ , and (e-f) EDS images of  $g\text{-C}_3\text{N}_4/\text{PANI}$  (3%) (The white arrows of the Figure 2(b) denote the PAN and  $g\text{-C}_3\text{N}_4$ , respectively).

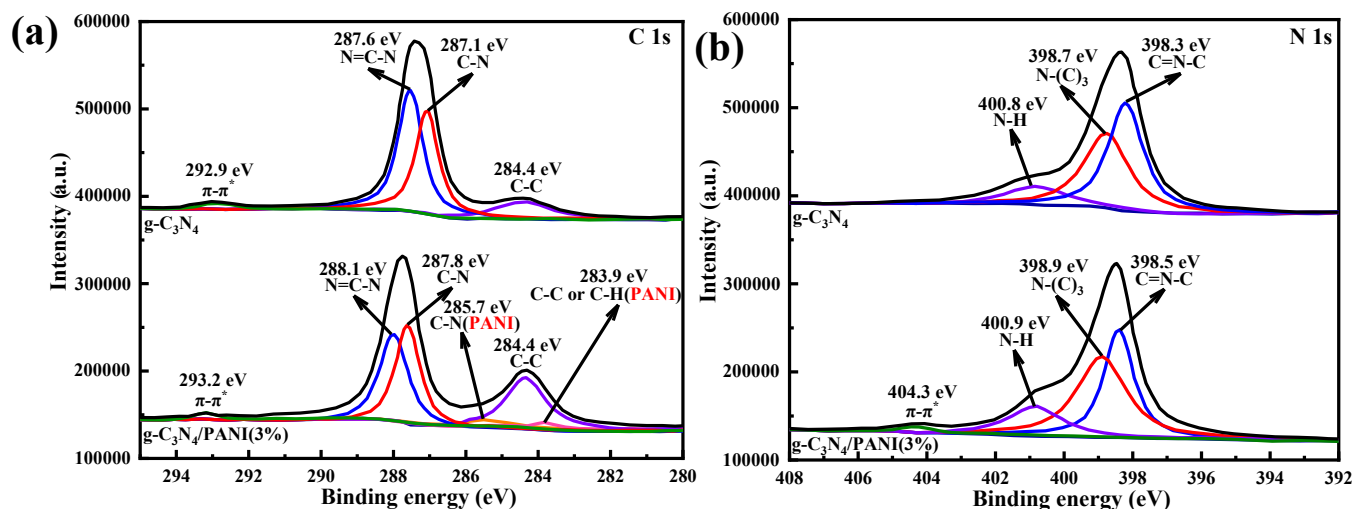


Figure 3. (a) XPS spectrum of C 1s and (b) N 1s of g-C<sub>3</sub>N<sub>4</sub> and g-C<sub>3</sub>N<sub>4</sub>/PANI(3%).

As Figure 3(b) shows, the binding energies of 398.3, 398.7, and 400.8 eV correspond to the C=N-C, N-(C)<sub>3</sub>, and N-H group, respectively. The g-C<sub>3</sub>N<sub>4</sub> is wrapped by the conductive polymer PANI. A new characteristic peak appears near the binding energy of 404.3 eV, attributed to the presence of π-π\* conjugation [36]. N 1s characteristic peak position of g-C<sub>3</sub>N<sub>4</sub>/PANI exhibits a shift toward higher binding energy compared to g-C<sub>3</sub>N<sub>4</sub>. This result indicates the presence of an interaction between the PANI and g-C<sub>3</sub>N<sub>4</sub>. The above results indicate that the heterojunction is formed in the g-C<sub>3</sub>N<sub>4</sub>/PANI.

### 3.4. Pore structure analysis

Table 1 presents the pore structure data of PANI, g-C<sub>3</sub>N<sub>4</sub>, and g-C<sub>3</sub>N<sub>4</sub>/PANI. As shown, the specific surface area of PANI and g-C<sub>3</sub>N<sub>4</sub> is 80.21 and 21.31 m<sup>2</sup>·g<sup>-1</sup>, respectively (Table 1). This result indicates that the surface area of g-C<sub>3</sub>N<sub>4</sub>/PANI decreases compared to PANI after incorporating PANI with g-C<sub>3</sub>N<sub>4</sub>. The pore volume and average pore diameter of g-C<sub>3</sub>N<sub>4</sub> are 0.20 cm<sup>3</sup>·g<sup>-1</sup> and 16.22 nm, respectively. After the coupling between g-C<sub>3</sub>N<sub>4</sub> and PANI to form a heterojunction, the pore volume and average pore diameter significantly improved. The increase in pore volume and average pore diameter is beneficial to the material's adsorption of CO<sub>2</sub> and the diffusion of CO<sub>2</sub> in the pore structure. The reason for this result may be that the coupling between PANI and g-C<sub>3</sub>N<sub>4</sub> forms a heterojunction, which leads to the local reconstruction of the layered structure of g-C<sub>3</sub>N<sub>4</sub>, thus achieving an increase in pore volume and pore diameter.

### 3.5. UV-visible diffuse reflectance spectrum analysis

The UV-vis diffuse reflectance spectrum (DRS) was used to investigate the spectral response of g-C<sub>3</sub>N<sub>4</sub>, PANI, and g-C<sub>3</sub>N<sub>4</sub>/PANI (3%). As displayed in Figure 4(a), the g-C<sub>3</sub>N<sub>4</sub>, PANI, and g-C<sub>3</sub>N<sub>4</sub>/PANI exhibit absorption responses in both the ultraviolet and visible light regions. Cutoff wavelengths of g-C<sub>3</sub>N<sub>4</sub>, PANI, and g-C<sub>3</sub>N<sub>4</sub>/PANI are 478, 585, and 548 nm, respectively. The absorption boundary of g-C<sub>3</sub>N<sub>4</sub>/PANI is significantly red-shifted, and the spectral absorption range is

Table 1. Pore structure data of the PANI, g-C<sub>3</sub>N<sub>4</sub>, and g-C<sub>3</sub>N<sub>4</sub>/PANI.

Sample	Specific surface area (m <sup>2</sup> ·g <sup>-1</sup> )	Pore volume (cm <sup>3</sup> ·g <sup>-1</sup> )	Average pore size (nm)
PANI	80.21	0.35	21.75
g-C <sub>3</sub> N <sub>4</sub>	21.31	0.20	16.22
g-C <sub>3</sub> N <sub>4</sub> /PANI (1%)	68.48	0.46	34.33
g-C <sub>3</sub> N <sub>4</sub> /PANI (3%)	66.13	0.46	35.01
g-C <sub>3</sub> N <sub>4</sub> /PANI (5%)	60.34	0.45	35.14

broadened, contributing to improving its photocatalytic performance. This phenomenon is closely associated with heterojunction interaction between PANI and g-C<sub>3</sub>N<sub>4</sub> [37]. From the Tauc curve in Figure 4(b), it can be obtained that the band gap energies ( $E_g$ ) of g-C<sub>3</sub>N<sub>4</sub>, PANI, and g-C<sub>3</sub>N<sub>4</sub>/PANI (3%) were 2.61, 2.13, and 2.50 eV, respectively. This result indicates that the band gap energy reduced after coupling between g-C<sub>3</sub>N<sub>4</sub> and PANI to form a heterojunction, which broadened the visible light spectrum absorption range [38]. Therefore, the photocatalytic performance improved.

### 3.6. Fluorescence spectrum analysis

The photogenerated carrier separation, recombination, and lifetime of g-C<sub>3</sub>N<sub>4</sub> and g-C<sub>3</sub>N<sub>4</sub>/PANI(3%) were analyzed using photoluminescence (PL) and time-resolved photoluminescence (TRPL) spectroscopy (Figure 5). As Figure 5(a) shows, the g-C<sub>3</sub>N<sub>4</sub> has a large typical emission peak intensity, indicating that g-C<sub>3</sub>N<sub>4</sub> exhibits high photogenerated carrier recombination. This phenomenon is the primary factor limiting the photocatalytic performance of g-C<sub>3</sub>N<sub>4</sub>. When the conductive polymer PANI wraps g-C<sub>3</sub>N<sub>4</sub>, the typical emission peak intensity of the g-C<sub>3</sub>N<sub>4</sub>/PANI reduces. This reduction effectively suppresses photogenerated carrier recombination in the g-C<sub>3</sub>N<sub>4</sub>/PANI, which can be explained by the interaction at the heterojunction between PANI and g-C<sub>3</sub>N<sub>4</sub>. As Figure 5(b) shows, the average photogenerated carrier lifetime of g-C<sub>3</sub>N<sub>4</sub>/PANI and g-C<sub>3</sub>N<sub>4</sub> is 6.18 and 4.97 ns, respectively. This phenomenon can be attributed to the excellent electrical conductivity of the conductive polymer PANI, which facilitates the transfer of excited-state photoelectrons to the interface and effectively inhibits photogenerated carriers' recombination [39]. The effective separation and prolonged lifetime of photogenerated carriers are attributed to the heterogeneous interactions.

### 3.7. Electrochemical property analysis

The transient photocurrent and electrochemical impedance spectroscopy (EIS) of g-C<sub>3</sub>N<sub>4</sub> and g-C<sub>3</sub>N<sub>4</sub>/PANI(3%) were characterized using transient photocurrent (TPC) measurements and EIS, with the results presented in Figure 6. As Figure 6(a) shows, g-C<sub>3</sub>N<sub>4</sub> and the g-C<sub>3</sub>N<sub>4</sub>/PANI exhibit stable photocurrents during three cycling periods. Notably, the transient photocurrent intensity is significantly enhanced after encapsulation of g-C<sub>3</sub>N<sub>4</sub> with the conductive polymer PANI. This result indicates that the charge transfer rate significantly increases due to the rapid migration of photoelectrons generated by light-driven charge separation in g-C<sub>3</sub>N<sub>4</sub>, following its encapsulation by the conductive polymer PANI. These photoelectrons efficiently migrate to the conductive interface and subsequently to the surface of g-C<sub>3</sub>N<sub>4</sub> [40]. The g-C<sub>3</sub>N<sub>4</sub>/PANI exhibits significantly smaller AC impedance radius than pristine g-C<sub>3</sub>N<sub>4</sub> (Figure 6b). The charge transfer resistance

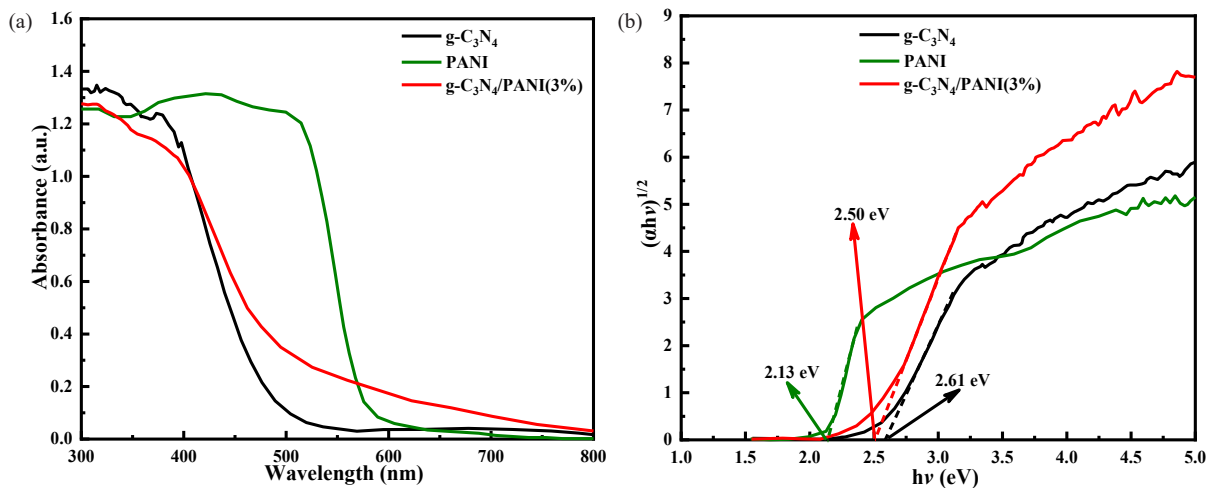


Figure 4. (a) UV-vis DRS spectrum and (b) Tauc plot of g-C<sub>3</sub>N<sub>4</sub>, PANI, and g-C<sub>3</sub>N<sub>4</sub>/PANI(3%).

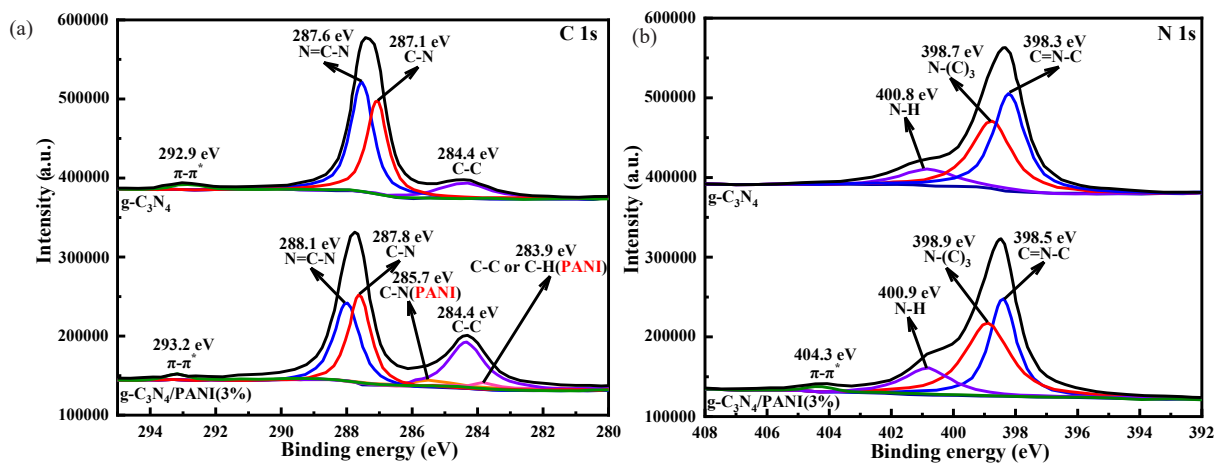


Figure 5. (a) PL and (b) TRPL spectrum of g-C<sub>3</sub>N<sub>4</sub> and g-C<sub>3</sub>N<sub>4</sub>/PANI (3%).

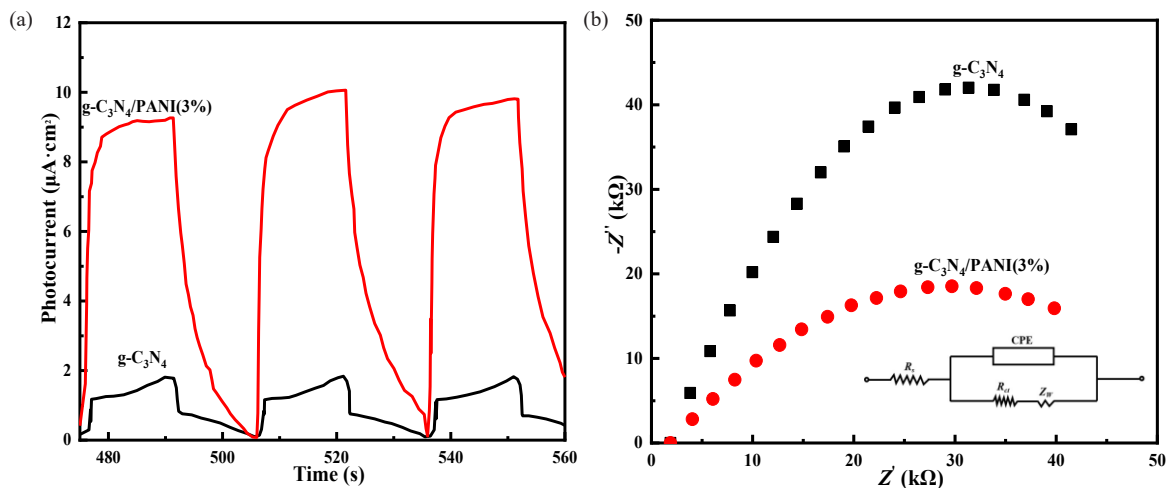


Figure 6. (a) TPC and (b) EIS spectrum of g-C<sub>3</sub>N<sub>4</sub> and g-C<sub>3</sub>N<sub>4</sub>/PANI(3%).

$R_{ct}$  of g-C<sub>3</sub>N<sub>4</sub>/PANI and g-C<sub>3</sub>N<sub>4</sub> is 45.1 and 199.2  $\Omega$  in the inset of Figure 6(b), respectively. This result indicates that the conductivity of the conductive polymer PANI encapsulating the g-C<sub>3</sub>N<sub>4</sub> significantly increases. Therefore, the separation rate of photogenerated carriers is effectively improved due to the formed heterojunction between PANI and g-C<sub>3</sub>N<sub>4</sub> [41]. The excellent electrochemical properties of g-C<sub>3</sub>N<sub>4</sub>/PANI are conducive to enhancing its photocatalytic performance.

### 3.8. CO<sub>2</sub> photoreduction performance for production of CH<sub>3</sub>OH

Figure 7 shows the product yields of the CO<sub>2</sub> photoreduction process using g-C<sub>3</sub>N<sub>4</sub> and g-C<sub>3</sub>N<sub>4</sub>/PANI, and the CH<sub>3</sub>OH yield of g-C<sub>3</sub>N<sub>4</sub>/PANI(3%) after five cycles. As Figure 7(a) shows, the pure g-C<sub>3</sub>N<sub>4</sub> exhibits low yields of 0.73 and 0.06  $\mu\text{mol}\cdot\text{g}^{-1}\cdot\text{h}^{-1}$  for CH<sub>3</sub>OH and CO during the CO<sub>2</sub> photoreduction process, respectively. It may be attributed to the

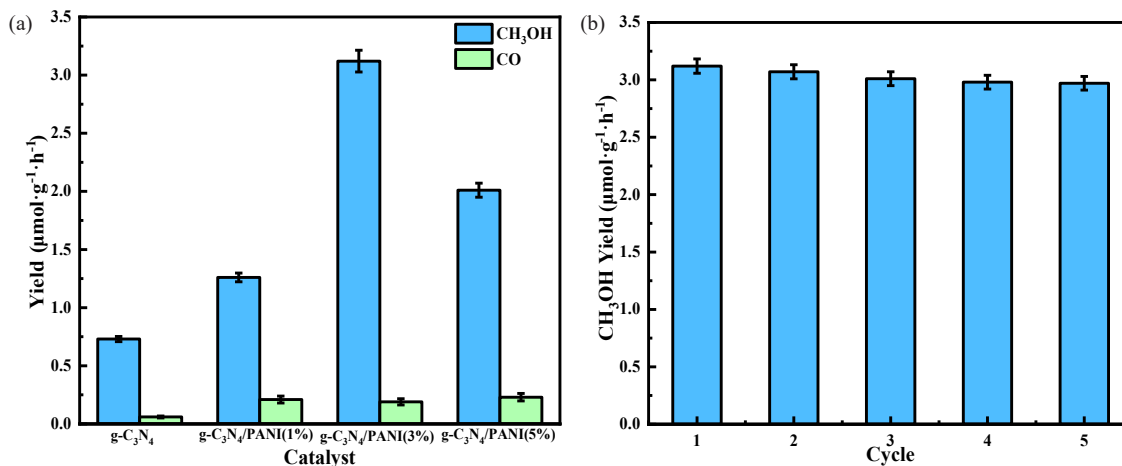


Figure 7. The yields of (a) CO<sub>2</sub> photoreduction products and (b) CH<sub>3</sub>OH after five cycles (g-C<sub>3</sub>N<sub>4</sub>/PANI (3%): 50 mg, CO<sub>2</sub>: 1.0 atm).

relatively fast recombination rate of photogenerated carriers. The CH<sub>3</sub>OH and CO yield of g-C<sub>3</sub>N<sub>4</sub>/PANI significantly increases. The reason is that the PANI layer enhances CO<sub>2</sub> adsorption and electron delivery. Besides, the light utilization and charge separation rate of the g-C<sub>3</sub>N<sub>4</sub>/PANI improved. The formed heterojunction in g-C<sub>3</sub>N<sub>4</sub>/PANI also effectively promotes photogenerated carriers separation. The CH<sub>3</sub>OH yields of g-C<sub>3</sub>N<sub>4</sub>/PANI(1%), g-C<sub>3</sub>N<sub>4</sub>/PANI(3%), and g-C<sub>3</sub>N<sub>4</sub>/PANI(5%) were 1.26, 3.12, and 2.01 μmol·g<sup>-1</sup>·h<sup>-1</sup>, respectively. While CO yields of g-C<sub>3</sub>N<sub>4</sub>/PANI(1%), g-C<sub>3</sub>N<sub>4</sub>/PANI(3%), and g-C<sub>3</sub>N<sub>4</sub>/PANI(5%) were 0.21, 0.19, and 0.23 μmol·g<sup>-1</sup>·h<sup>-1</sup>, respectively. Above results indicate that g-C<sub>3</sub>N<sub>4</sub>/PANI(3%) exhibits excellent CO<sub>2</sub> photoreduction performance compared to other PANI contents. The CH<sub>3</sub>OH yield of the g-C<sub>3</sub>N<sub>4</sub>/PANI(3%) is 4.23 times larger than g-C<sub>3</sub>N<sub>4</sub>. When conductive polymer PANI content is low, the heterojunction is not easy to be formed in g-C<sub>3</sub>N<sub>4</sub>/PANI, which consequently hinders effective separation of photogenerated carriers. When PANI content is high, the g-C<sub>3</sub>N<sub>4</sub> is sufficiently wrapped, and the effective contact between the conductive polymer PANI and the g-C<sub>3</sub>N<sub>4</sub> is significantly restricted. Therefore, the CO<sub>2</sub> photoreduction performance is poor. These results also indicate that the formed heterojunction can effectively promote photogenerated carriers separation and improve CO<sub>2</sub> photoreduction performance for production of CH<sub>3</sub>OH. Besides, the CH<sub>3</sub>OH yield of the g-C<sub>3</sub>N<sub>4</sub>/PANI is higher than that of the CO. This result indicates that g-C<sub>3</sub>N<sub>4</sub>/PANI exhibits higher selectivity towards CH<sub>3</sub>OH production compared to CO production.

Furthermore, the stability of photocatalytic materials is another critical factor influencing their practical applications. The CH<sub>3</sub>OH yield of the g-C<sub>3</sub>N<sub>4</sub>/PANI(3%) is 2.97 μmol·g<sup>-1</sup>·h<sup>-1</sup> after five cycles, maintaining 95% CO<sub>2</sub> photoreduction performance. This analysis indicates that g-C<sub>3</sub>N<sub>4</sub>/PANI(3%) exhibits excellent stability, contributing to actual application.

### 3.9. Analysis of CO<sub>2</sub> photoreduction mechanism

The energy band potential is very important for the analysis of the charge transfer mechanism and the photocatalytic mechanism. The Tauc curve in Figure 4(b) shows that the band gap energies ( $E_g$ ) of g-C<sub>3</sub>N<sub>4</sub> and PANI were 2.61 and 2.13 eV, respectively. From the VB-XPS spectrum in Figure 8, it can be obtained that the valence band potentials ( $E_{VB}$ ) of g-C<sub>3</sub>N<sub>4</sub> and PANI were 1.54 and 1.61 eV, respectively. Based on the calculation method of  $E_g = E_{VB} - E_{CB}$ , the conduction band potential ( $E_{CB}$ ) of g-C<sub>3</sub>N<sub>4</sub> and PANI were determined to be -1.07 and -0.52 eV, respectively.

Based on the energy band structure, the Z-type charge transfer mechanism and g-C<sub>3</sub>N<sub>4</sub>/PANI photocatalytic reduction of CO<sub>2</sub> mechanism in Figure 9 were obtained. Under the irradiation of visible light ( $\lambda > 420$  nm), the photocatalytic material g-C<sub>3</sub>N<sub>4</sub> and the conductive polymer PANI undergoes charge separation, generating photoelectrons ( $e^-$ ) and holes ( $h^+$ ). The  $e^-$  transition occurs and migrates from the valence band (VB) to the conduction band (CB), causing CB to generate

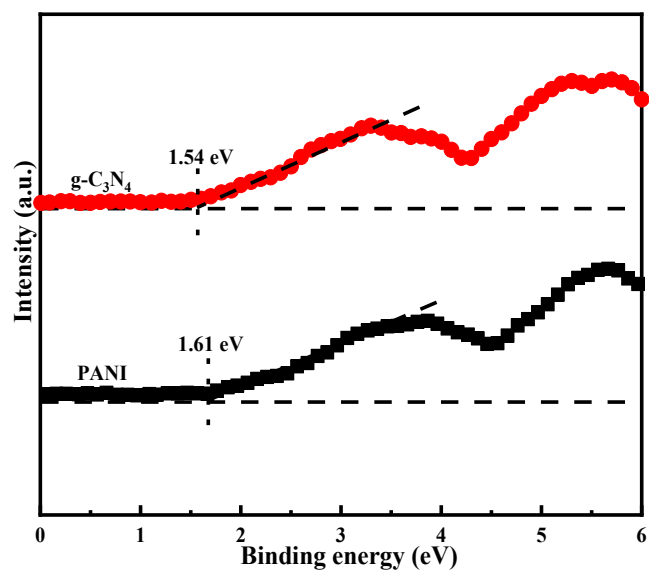


Figure 8. VB-XPS spectrum of g-C<sub>3</sub>N<sub>4</sub> and PANI.

a large amount of  $h^+$ . Because of the difference in the energy band positions between g-C<sub>3</sub>N<sub>4</sub> and PANI, the CB position  $e^-$  of g-C<sub>3</sub>N<sub>4</sub> will transition to the CB position of PANI, and the VB position  $h^+$  of PANI will transition to the VB position of g-C<sub>3</sub>N<sub>4</sub>. The CB potential of PANI is more negative than the standard hydrogen electrode potential (SHE) of CO<sub>2</sub>/CH<sub>3</sub>OH. There is a significant thermodynamic potential difference, enabling electrons to readily reduce CO<sub>2</sub> to CH<sub>3</sub>OH. However, the test results show that the products of g-C<sub>3</sub>N<sub>4</sub>/PANI heterojunction catalytic reduction of CO<sub>2</sub> are CH<sub>3</sub>OH and CO. Therefore, the charge transfer path of g-C<sub>3</sub>N<sub>4</sub>/PANI heterojunction does not conform to the type II charge transfer mechanism [42]. Therefore, a Z-type charge transfer mechanism is proposed. The  $e^-$  at the CB position of PANI migrates to the VB position of g-C<sub>3</sub>N<sub>4</sub>. A large amount of  $h^+$  remains at the VB position of PANI, and a large amount of  $e^-$  remains at the CB position of g-C<sub>3</sub>N<sub>4</sub>, achieving efficient photogenerated carrier separation [43]. The CB potential of g-C<sub>3</sub>N<sub>4</sub> is more negative than the SHE potential of O<sub>2</sub>/·O<sub>2</sub><sup>-</sup>. Thermodynamically, electrons at the conduction band (CB) position can reduce O<sub>2</sub> to form highly reactive superoxide radicals (·O<sub>2</sub><sup>-</sup>). The VB potential of PANI is more negative than the SHE potential of H<sub>2</sub>O/·OH and the SHE potential of H<sub>2</sub>O/O<sub>2</sub>. Thermodynamically, the  $h^+$  at the VB position cannot oxidize H<sub>2</sub>O to hydroxyl radicals (·OH). While, it can oxidize H<sub>2</sub>O to O<sub>2</sub> and H<sup>+</sup>. The CB potential of g-C<sub>3</sub>N<sub>4</sub> is more negative than the SHE potential of CO<sub>2</sub>/CO and CO<sub>2</sub>/CH<sub>3</sub>OH. With the cooperation of the active free radical ·O<sub>2</sub><sup>-</sup>, the  $e^-$  at the CB position reduces CO<sub>2</sub> to the main product CH<sub>3</sub>OH and the by-product

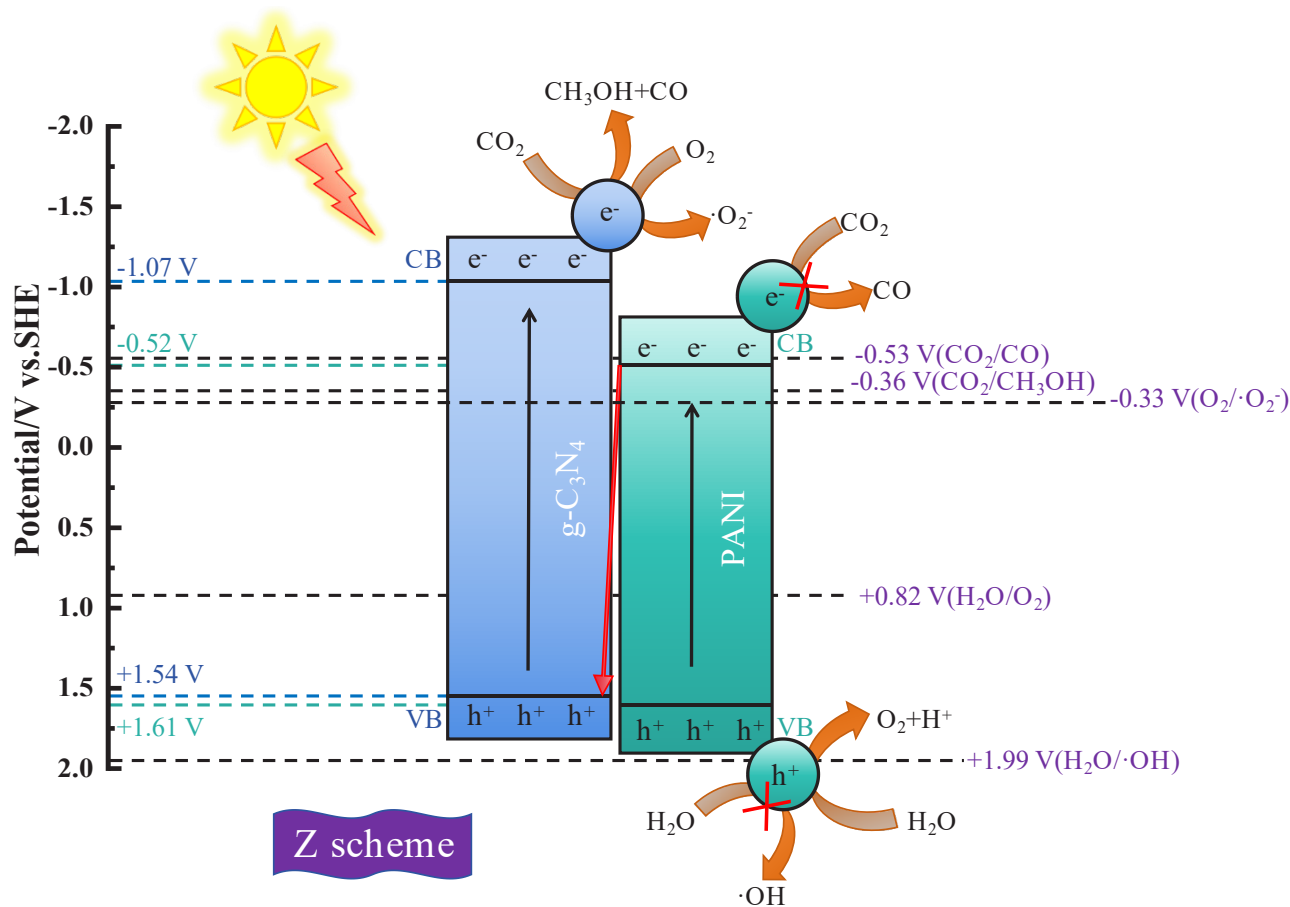


Figure 9. Z-scheme charge transfer mechanism and photocatalytic reduction of CO<sub>2</sub> mechanism of g-C<sub>3</sub>N<sub>4</sub>/PANI heterojunction.

CO. Besides, this reaction shows high selectivity. The Z-type charge transfer mechanism of g-C<sub>3</sub>N<sub>4</sub>/PANI effectively promotes the separation of photogenerated carriers and broadens the visible light spectrum absorption range. The CB position of g-C<sub>3</sub>N<sub>4</sub> retains highly reducing active e<sup>-</sup>, achieving efficient reduction of CO<sub>2</sub> [44].

#### 4. Conclusions

The g-C<sub>3</sub>N<sub>4</sub>/PANI was synthesized by constructing heterojunction strategy using aniline and g-C<sub>3</sub>N<sub>4</sub> as precursors. The g-C<sub>3</sub>N<sub>4</sub> was wrapped by the conductive polymer PANI to form a heterojunction, realizing efficient photoelectron-hole separation and rapid charge transfer. The photocatalytic reduction of CO<sub>2</sub> by g-C<sub>3</sub>N<sub>4</sub>/PANI was superior to that of g-C<sub>3</sub>N<sub>4</sub>. CH<sub>3</sub>OH and CO yields of the g-C<sub>3</sub>N<sub>4</sub>/PANI (3%) were 3.12 and 0.19 μmol·g<sup>-1</sup>·h<sup>-1</sup>, respectively, showing high selectivity of CH<sub>3</sub>OH production. The selectivity of CH<sub>3</sub>OH production was as high as 95.26%. A meticulously engineered g-C<sub>3</sub>N<sub>4</sub>/PANI heterojunction can significantly enhance charge separation and expedite the migration of photogenerated electrons. CO<sub>2</sub> photoreduction mechanism of g-C<sub>3</sub>N<sub>4</sub>/PANI is investigated. The prepared g-C<sub>3</sub>N<sub>4</sub>/PANI has potential application in greenhouse gas CO<sub>2</sub> reduction for production of CH<sub>3</sub>OH as energy fuel.

#### CRedit authorship contribution statement

**Yujuan Liu:** Writing - review & editing, Methodology, Investigation. **Suping Wang:** Resources, Formal analysis, Visualization. **Kejun Bi:** Writing-original draft, Resources, Investigation, Supervision. **Yapo Sun:** Resources, Formal analysis.

#### Data availability

Data will be made available on request.

#### Declaration of competing interest

There are no conflicts of interest.

#### Declaration of generative AI and AI-assisted technologies in the writing process

The authors confirm that there was no use of artificial intelligence (AI)-assisted technology for assisting in the writing or editing of the manuscript and no images were manipulated using AI.

#### Acknowledgment

The authors would like to express their gratitude to the Provincial Science and Technology Research and Development Program of Henan Province in 2025 Project: Research on the Failure Mechanism and Deformation Optimization Improvement Design of Expansion Joints in Prefabricated Highway Bridges (Project Number: 252102241016) for financial support.

#### References

- Cheng, S., Tao, C., Li, H., 2025. Preparation of carbon nanotubes from organic solid wastes: A review. *Journal of Analytical and Applied Pyrolysis*, 192, 107240. <https://doi.org/10.1016/j.jaap.2025.107240>
- Mo, J., Liu, S., Xu, Q.Q., He, X.Y., Mu, W.H., Teng, M.Y., Fu, W.F., 2025. Pt single atoms promoting the construction of asymmetric double sites to achieve highly selective photoreduction of CO<sub>2</sub> to ethylene. *Journal of Colloid and Interface Science*, 683, 301-309. <https://doi.org/10.1016/j.jcis.2024.12.130>
- Nouri, A., Hasanzadeh, A., Chitsaz, A., Rosen, A.M., Khalilian, M., 2025. Comparison of various CO<sub>2</sub> capture strategies for five optimized fuel-to-power systems based on solid oxide fuel cells: Technical, economic, and environmental analyses. *Energy*, 317, 134683. <https://doi.org/10.1016/j.energy.2025.134683>

4. Su, X., Xu, Z., Li, M., Zhong, J., 2025. HF acid treatment induced nitrogen vacancies enriched g-C<sub>3</sub>N<sub>4</sub> for efficient photocatalytic CO<sub>2</sub> reduction and hydrogen production. *Chemical Physics Letters*, **861**, 141818. <https://doi.org/10.1016/j.cplett.2024.141818>
5. Foroughipour, M., Nezamzadeh-Ejehieh, A., 2023. CaTiO<sub>3</sub>/g-C<sub>3</sub>N<sub>4</sub> heterojunction-based composite photocatalyst: Part I: Experimental design, kinetics and scavenging agents effects in photocatalytic degradation of gemifloxacin. *Chemosphere*, **334**, 139019. <https://doi.org/10.1016/j.chemosphere.2023.139019>
6. Rezaei, M., Nezamzadeh-Ejehieh, A., Massah, A.R., 2025. A comprehensive review on the boosted effects of anion vacancy in the photocatalytic and photoelectrochemical water-splitting: Focus on oxygen vacancy. *Materials Today Energy*, **48**, 101754. <https://doi.org/10.1016/j.mtener.2024.101754>
7. Shi, S., Jia, M., Li, M., Zhou, S., Zhao, Y., Zhong, J., Dai, D., Qiu, J., 2023. ZnO@g-C<sub>3</sub>N<sub>4</sub> S-scheme photocatalytic membrane with visible-light response and enhanced water treatment performance. *Colloids and Surfaces A: Physicochemical and Engineering Aspects*, **667**, 131259. <https://doi.org/10.1016/j.colsurfa.2023.131259>
8. Zhang, S., Rong, X., Sun, T., Gao, P., Liu, J., Qiu, X., Zhou, X., Wu, Z., 2023. Construct vacancy nitrogen controllable Z-scheme 3D porous g-C<sub>3</sub>N<sub>4</sub>/CoFe<sub>2</sub>O<sub>4</sub> composite material for high-efficient photofixation nitrogen. *Diamond and Related Materials*, **138**, 110167. <https://doi.org/10.1016/j.diamond.2023.110167>
9. Pourshirband, N., Nezamzadeh-Ejehieh, A., Mirsattari, S.N., 2021. The CdS/g-C<sub>3</sub>N<sub>4</sub> nano-photocatalyst: Brief characterization and kinetic study of photodegradation and mineralization of methyl orange. *Spectrochimica Acta. Part A, Molecular and Biomolecular Spectroscopy*, **248**, 119110. <https://doi.org/10.1016/j.saa.2020.119110>
10. Deng, Y., Li, L., Zeng, H., Tang, R., Zhou, Z., Sun, Y., Feng, C., Gong, D., Wang, J., Huang, Y., 2023. Unveiling the origin of high-efficiency charge transport effect of C<sub>3</sub>N<sub>4</sub>/C<sub>3</sub>N<sub>4</sub> homojunction for activating peroxymonosulfate to degrade atrazine under visible light. *Chemical Engineering Journal*, **457**, 141261. <https://doi.org/10.1016/j.cej.2022.141261>
11. Thanh Truc, N.T., Pham, T.D., Nguyen, M.V., Van Thuan, D., Trung, D.Q., Thao, P., Trang, H.T., Nguyen, V.N., Tran, D.T., Minh, D.N., Hanh, N.T., Ngoc, H.M., 2020. Advanced NiMoO<sub>4</sub>/g-C<sub>3</sub>N<sub>4</sub> Z-scheme heterojunction photocatalyst for efficient conversion of CO<sub>2</sub> to valuable products. *Journal of Alloys and Compounds*, **842**, 155860. <https://doi.org/10.1016/j.jallcom.2020.155860>
12. Ikreedegh, R.R., Tasleem, S., Hossen, M.A., 2024. Facile fabrication of binary g-C<sub>3</sub>N<sub>4</sub>/NH<sub>2</sub>-MIL-125(Ti) MOF nanocomposite with Z-scheme heterojunction for efficient photocatalytic H<sub>2</sub> production and CO<sub>2</sub> reduction under visible light. *Fuel*, **360**, 130561. <https://doi.org/10.1016/j.fuel.2023.130561>
13. Qin, X., Zeng, X., Cheng, S., Xing, B., Shi, C., Yi, G., Nie, Y., Wang, Q., Zhang, C., Xia, H., 2023. Preparation of double functional carbon-based ZnO derived from rape straw for dye wastewater treatment. *Journal of Water Process Engineering*, **52**, 103588. <https://doi.org/10.1016/j.jwpe.2023.103588>
14. Saeed, M., Asghar, H., Khan, I., Akram, N., Usman, M., 2025. Synthesis of TiO<sub>2</sub>-g-C<sub>3</sub>N<sub>4</sub> for efficient photocatalytic degradation of Congo Red dye. *Catalysis Today*, **447**, 115154. <https://doi.org/10.1016/j.cattod.2024.115154>
15. Xiao, X., Wang, M., Huang, M., Liang, Y., Fan, Y., Wei, L., Xiong, J., Liang, Y., 2025. Efficient synergistic catalytic degradation of naphthalene in water by g-C<sub>3</sub>N<sub>4</sub>/ZnO heterojunction immobilized lipase. *Separation and Purification Technology*, **360**, 130990. <https://doi.org/10.1016/j.seppur.2024.130990>
16. Yu, S., Li, P., Ding, H., Ma, X., 2024. Construction of high-performance g-C<sub>3</sub>N<sub>4</sub>/MoS<sub>2</sub> heterojunction humidity sensor and investigation of its application. *Sensors and Actuators B: Chemical*, **419**, 136392. <https://doi.org/10.1016/j.snb.2024.136392>
17. Song, Z., Song, S., Zhang, W., Liu, D., Wang, Q., Wu, D., Ma, C., Feng, S., 2025. Multifunctional g-C<sub>3</sub>N<sub>4</sub>-PDI/MOF-545-NH<sub>2</sub> photocatalyst for enhanced CO<sub>2</sub> reduction and aniline oxidation. *Separation and Purification Technology*, **353**, 128174. <https://doi.org/10.1016/j.seppur.2024.128174>
18. Ma, W., Zhu, Y., Wang, X., 2023. Au nanoparticles modified HNTs/g-C<sub>3</sub>N<sub>4</sub>/CdS composite for highly efficient CO<sub>2</sub> photoreduction and tetracycline degradation. *Journal of Alloys and Compounds*, **935**, 168129. <https://doi.org/10.1016/j.jallcom.2022.168129>
19. Saleem, S.U., Pang, Z., Liu, Y., Sui, J., Waterhouse, G.I.N., Zhang, Z., Yu, L., 2025. Highly sensitive electrochemical sensor for lead ions based on Bi-MOF/conducting polymer composites. *Chemosphere*, **370**, 144019. <https://doi.org/10.1016/j.chemosphere.2024.144019>
20. Camlibel, N.O., Kandola, B.K., 2025. Highly sensitive textile pressure sensors with novel hierarchical architecture based on conductive polymers, silver nanoparticles and carbon nanotubes. *Sensors and Actuators A: Physical*, **382**, 116166. <https://doi.org/10.1016/j.sna.2024.116166>
21. Ahmer, M.F., Ullah, Q., Uddin, M.K., 2025. Magnetic metal oxide assisted conducting polymer nanocomposites as eco-friendly electrode materials for supercapacitor applications: A review. *Journal of Polymer Engineering*, **45**, 1-41. <https://doi.org/10.1515/polyeng-2024-0101>
22. Saraei, H., Tanzifi, M., Mansouri, M., Saraei, M., Tavakkoli Yaraki, M., 2025. Fabrication of a novel Z-scheme 2D/1D g-C<sub>3</sub>N<sub>4</sub>/polyaniline decorated on activated carbon with effective visible-light photocatalytic activity. *Environmental Research*, **267**, 120658. <https://doi.org/10.1016/j.envres.2024.120658>
23. Zhu, B., Zhou, J., Ni, L., Diao, G., 2025. Efficient photocatalytic elimination of antibiotics over metal-free CNx/PANI/graphene sponge system. *Solid State Sciences*, **159**, 107781. <https://doi.org/10.1016/j.solidstatedsciences.2024.107781>
24. Miao, S., Huang, M., Chen, C., Hu, W., Wang, S., Li, B., 2023. Photoinduced deposition of AuCu cocatalyst and polyaniline conducting layer on graphitic-C<sub>3</sub>N<sub>4</sub> for enhanced CO<sub>2</sub> photoreduction. *Colloids and Surfaces A: Physicochemical and Engineering Aspects*, **670**, 131584. <https://doi.org/10.1016/j.colsurfa.2023.131584>
25. Aroui, L., Madani, S., Bousnoubra, I., Boublia, A., Lakikza, I., Aouni, S.I., Abdelouahed, L., Ernst, B., Alam, M., Benguerba, Y., 2024. Enhanced degradation of crystal violet using PANI-ZnO nanocomposites: Electro-oxidation and photocatalysis studies. *Journal of Molecular Liquids*, **412**, 125818. <https://doi.org/10.1016/j.molliq.2024.125818>
26. Zhang, Y., Gao, Y., Deng, R., Qin, Z., Shi, F., Zeng, J., Zhao, C., Pu, Y., Duan, T., 2025. Effective charge separation in CdS@PANI heterostructure for ultrafast visible light-driven photocatalytic reduction of uranium(VI). *Separation and Purification Technology*, **354**, 129331. <https://doi.org/10.1016/j.seppur.2024.129331>
27. Shi, L., Liu, G., Zhang, Y., Yang, Z., 2023. Na, O co-doping and cyano groups synergistically adjust the band structure of g-C<sub>3</sub>N<sub>4</sub> for improving photocatalytic oxygen evolution. *Materials Research Bulletin*, **167**, 112423. <https://doi.org/10.1016/j.materresbull.2023.112423>
28. Mao, J., Wang, J., Zhang, J., Shi, S., Zhang, Y., Bai, Y., Qu, J., 2025. Interfacial charge steering in CdS/nitrogen-deficient g-C<sub>3</sub>N<sub>4</sub> heterojunctions boosts solar-driven persulfate activation for PPCPs decontamination. *Separation and Purification Technology*, **377**, 134480. <https://doi.org/10.1016/j.seppur.2025.134480>
29. Foroughipour, M., Nezamzadeh-Ejehieh, A., 2024. CaTiO<sub>3</sub> perovskite/g-C<sub>3</sub>N<sub>4</sub> heterojunction-based composite photocatalyst, part II: Synthesis, characterization and the boosted photocatalytic activity towards Gemifloxacin. *Diamond and Related Materials*, **141**, 110711. <https://doi.org/10.1016/j.diamond.2023.110711>
30. Wu, E., Zhang, J., Cai, M., Bai, J., Xue, J., Jiang, Y., Chen, J., Mao, C.J., Sun, S., 2025. Polyaniline as a solid-state charge conductor for enhanced photocatalytic hydrogen production and value-added disulfide synthesis. *Separation and Purification Technology*, **354**, 129250. <https://doi.org/10.1016/j.seppur.2024.129250>
31. Tamiji, T., Nezamzadeh-Ejehieh, A., 2019. Study of kinetics aspects of the electrocatalytic oxidation of benzyl alcohol in aqueous solution on AgBr modified carbon paste electrode. *Materials Chemistry and Physics*, **237**, 121813. <https://doi.org/10.1016/j.matchemphys.2019.121813>
32. Raesi-Kheirabadi, N., Nezamzadeh-Ejehieh, A., 2020. A Z-scheme g-C<sub>3</sub>N<sub>4</sub>/Ag<sub>3</sub>PO<sub>4</sub> nanocomposite: Its photocatalytic activity and capability for water splitting. *International Journal of Hydrogen Energy*, **45**, 33381-33395. <https://doi.org/10.1016/j.ijhydene.2020.09.028>
33. Sayed, M.A., Mohamed, A., Ahmed, S.A., El-Sherbeeney, A.M., Al Zoubi, W., Abukhadra, M.R., 2024. Enhanced photocatalytic degradation of Congo red dye into safe end-products over ZnO@polyaniline/coal composite as low cost catalyst under visible light: Pathways and ecotoxicity. *Journal of Photochemistry and Photobiology A: Chemistry*, **456**, 115843. <https://doi.org/10.1016/j.jphotochem.2024.115843>
34. Liu, S., Xu, T., Zhu, L., Liu, K., Ji, X., Yuan, Z., Si, C., 2025. Highly compressible ultralight 3D cellulose/graphene/carbon nitride aerogel for enhanced photocatalytic activity. *Chemical Engineering Journal*, **503**, 158564. <https://doi.org/10.1016/j.cej.2024.158564>
35. Benaouda, S.N., Chaker, H., Abidallah, F., Bachir, C., Tawheed, H., Weidler, P.G., Bengueddach, A., Canales-Vázquez, J., Hamacha, R., 2023. Heterogeneous photocatalytic degradation of anionic dye on polyaniline/microcrystalline cellulose composite. *Journal of Porous Materials*, **30**, 327-341. <https://doi.org/10.1007/s10934-022-01342-x>
36. Pan, X., Wu, S., Wang, T., Histan, G., Li, Y., 2022. Copper containing 3D polyaniline/phytic acid hydrogels for photocatalytic hydrogen production. *Journal of Materials Science*, **57**, 12836-12847. <https://doi.org/10.1007/s10853-022-07424-0>
37. Vahabirad, S., Nezamzadeh-Ejehieh, A., 2022. Co-precipitation synthesis of BiOI/(BiO)<sub>2</sub>CO<sub>3</sub>: Brief characterization and the kinetic study in the photodegradation and mineralization of sulfasalazine. *Journal of Solid State Chemistry*, **310**, 123018. <https://doi.org/10.1016/j.jssc.2022.123018>
38. Hemmatpour, P., Nezamzadeh-Ejehieh, A., 2022. A Z-scheme CdS/BiVO<sub>4</sub> photocatalysis towards Eriochrome black T: An experimental design and mechanism study. *Chemosphere*, **307**, 135925. <https://doi.org/10.1016/j.chemosphere.2022.135925>
39. Wang, L., Cheng, B., Zhang, L., Yu, J., 2021. In situ Irradiated XPS Investigation on S-Scheme TiO<sub>2</sub>@ZnIn<sub>2</sub>S<sub>4</sub> Photocatalyst for Efficient Photocatalytic CO<sub>2</sub> Reduction. *Small (Weinheim an der Bergstrasse, Germany)*, **17**, e2103447. <https://doi.org/10.1002/sml.202103447>
40. Amani-Beni, Z., Nezamzadeh-Ejehieh, A., 2018. NiO nanoparticles modified carbon paste electrode as a novel sulfasalazine sensor. *Analytica Chimica Acta*, **1031**, 47-59. <https://doi.org/10.1016/j.aca.2018.06.002>
41. Rezaei, M., Nezamzadeh-Ejehieh, A., Massah, A.R., 2024. A comprehensive review on the boosted effects of anion vacancy in the heterogeneous photocatalytic degradation, part I: Focus on sulfur, nitrogen, carbon, and halogen vacancies. *Ecotoxicology and Environmental Safety*, **269**, 115927. <https://doi.org/10.1016/j.ecoenv.2024.115927>
42. Mousavi, S.M., Mohtaram, M.S., Rasouli, K., Mohtaram, S., Rajabi, H., Sabbaghi, S., 2025. Efficient visible-light-driven photocatalytic degradation of antibiotics in water by MXene-derived TiO<sub>2</sub>-supported SiO<sub>2</sub>/Ti<sub>3</sub>C<sub>2</sub> composites: Optimisation, mechanism and toxicity evaluation. *Environmental Science and Pollution Research International (Barking, Essex : 1987)*, **367**, 125624. <https://doi.org/10.1016/j.envpol.2024.125624>
43. Zhu, Z., Ban, Y., Tang, L., Li, H., 2025. Construction of S-scheme heterojunction CeCuO<sub>4</sub>/g-C<sub>3</sub>N<sub>4</sub> photocatalyst for degradation of tetracycline under visible light. *Diamond and Related Materials*, **152**, 111888. <https://doi.org/10.1016/j.diamond.2024.111888>
44. Salei, S., Nezamzadeh-Ejehieh, A., 2023. An experimental design study of photocatalytic activity of the Z-scheme silver iodide/tungstate binary nano photocatalyst. *Environmental Science and Pollution Research International*, **30**, 105440-105456. <https://doi.org/10.1007/s11356-023-29730-z>